LAWRENCE
LIVERMORE
NATIONAL
LABORATORY

CT Results Using an Inverse Compton X-ray Source

S. Karimi, W. Brown, C. Thornton, Q. Chen, S. Glenn, M. Skeate, R. Jacob, K. Nakamura, T. Ostermayr, J. Tilborg, C. Geddes, H. Martz

April 11, 2023

Disclaimer

This document was prepared as an account of work sponsored by an agency of the United States government. Neither the United States government nor Lawrence Livermore National Security, LLC, nor any of their employees makes any warranty, expressed or implied, or assumes any legal liability or responsibility for the accuracy, completeness, or usefulness of any information, apparatus, product, or process disclosed, or represents that its use would not infringe privately owned rights. Reference herein to any specific commercial product, process, or service by trade name, trademark, manufacturer, or otherwise does not necessarily constitute or imply its endorsement, recommendation, or favoring by the United States government or Lawrence Livermore National Security, LLC. The views and opinions of authors expressed herein do not necessarily state or reflect those of the United States government or Lawrence Livermore National Security, LLC, and shall not be used for advertising or product endorsement purposes.

CT Results Using an Inverse Compton X-ray Source

Seemeen Karimi*[a], William Brown[a], Chris Thornton[b], Qiang Chen[c], Steven Glenn[a], Michael Skeate[a], Rob Jacob[c], Kei Nakamura[c], Tobias Ostermayr[c], Jeroen van Tilborg[c], Cameron Geddes[c], Harry Martz[a]

[a]Lawrence Livermore National Laboratory, 7000 East Ave, Livermore, CA, USA 94550; [b]Central Laser Facility, STFC Rutherford Appleton Laboratory, Harwell Campus Didcot, UK; [c]Lawrence Berkeley National Laboratory, 1 Cyclotron Rd, Berkeley, CA, USA 94720

ABSTRACT

Nondestructive characterization is often carried out on dense materials and objects, such as cargo, and high atomic number advanced manufactured, and traditionally manufactured parts and assemblies. These often require high-energy x-rays, exceeding 1 MeV, and sub-millimeter spatial resolution for characterization. Current high-energy x-ray systems offer limited flexibility in tuning the x-ray energy and spatial resolution. Current x-ray sources include bremsstrahlung tube heads that operate from 10 to 600 kV and accelerators that operate from 2 to 15 MV. The MV systems have spatial resolution on the order of a millimeter which limits the features that can be observed. An alternative approach is to use an inverse Compton scattering (ICS) x-ray source with a linear plasma accelerator (LPA). This is a powerful emerging technology that can provide tunable keV to MeV, quasi-monoenergetic x-rays, and a focal spot size on the order of a micrometer. Our research seeks to answer the question: can ICS x-ray sources fundamentally change the way x-ray non-destructive characterization (NDC) is carried out on these challenging parts, assemblies, and cargo? We performed the first CT scans using the Berkeley Lab Laser Accelerator Hundred TeraWatt (BELLA HTW) ICS x-ray source. We scanned parts of tungsten carbide and steel. Our reconstructed images, although they have artifacts, demonstrate the potential of the LPA-ICS source to image challenging objects. We will discuss the system used, results, lessons learned and paths forward.

Keywords: x-rays, computed tomography, nondestructive characterization, nondestructive evaluation, inverse Compton scattering, BELLA, laser plasma accelerator, laser wakefield acceleration

1. INTRODUCTION

In aerospace, automotive, and other industries, complex objects are manufactured from dense materials, such as Inconel [1], [2] and tungsten alloys [3][4]. The most effective nondestructive characterization (NDC) method for complex three-dimensional industrial parts is x-ray computed tomography (CT), due to its contrast resolution, spatial resolution, accessibility, 3D imaging, and cost. Quantitatively accurate CT imaging of these objects is challenging because it often simultaneously requires x-ray energies on the order of 1 MeV and sub-millimeter (mm) spatial resolution. X-ray sources are mainly of two kinds: x-ray tube or linear accelerator (Linac). X-ray tubes with micrometer focal spot size can be used to acquire sub-millimeter spatial resolution images but energies are under 600 keV. Linacs produce x-rays with energies in the MeV range but have 0.7-2 mm focal spots, and hence yield insufficient spatial resolution for structure metrology and defect detection [5]. X-ray tubes and linacs accelerate electrons toward a target. The electrons rapidly decelerate in the target producing a bremsstrahlung source of x-rays. These sources are polychromatic (have a wide energy spectrum), which degrades image quality when scanned objects harden the beam. Microtrons have micrometer-scale focal spots and high energies, but the x-rays are polychromatic [6]. Finally, energy-tunability is desirable to optimize the beam for various objects. The simultaneous need for sub-mm spatial resolution, MeV energies, narrow spectra and tunability necessitates the use of another x-ray source technology for NDC, for instance, an inverse Compton Source (ICS) x-ray source. ICS sources may be critical to advance NDC science for industry, national security [7][8], medical isotope production, archaeology, cargo imaging, and other fields.

*karimi1@llnl.gov; phone 1 617 953-1662; llnl.gov

In an inverse Compton scattering (ICS) x-ray source, low-energy photons from a laser pulse interact with a high-energy electron beam to generate x-rays, as illustrated in Figure 1. This method can generate MeV x-rays from an electron beam with energies on the order of 100 MeV. However, conventional accelerators required to generate such high-energy electron beams are large [9], limiting their use.
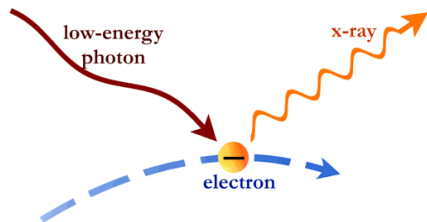
Figure 1. A low-energy photon, such as a light photon, interacts with a high-energy electron, producing an x-ray photon. Picture courtesy NASA : (https://chandra.harvard.edu/resources/illustrations/x-raysLight.html)

Laser plasma accelerators (LPA), also called laser wakefield accelerators, use a different principle to accelerate electron beams. In an LPA, a laser with a power density of 10^{18}-10^{19} W/cm^2 ionizes a gas, generating a plasma. The ponderomotive force of a short (c.a. 30 fs) pulse from a laser at this power density creates a plasma density wave (or wake) in the plasma that trails each laser pulse as it moves through the gas. This is called a wakefield, and has an order of 1 GeV/cm. Electron bunches are trapped in this wakefield and accelerate to relativistic energies within distances on the order of a centimeter. This allows the accelerator to be 3-4 orders of magnitude smaller than conventional accelerators, as well as potentially less costly. The electron beam created is typically a few micrometers [10],[11], and can be as small as 0.1 micrometer [12]. The LPA-ICS micrometer electron beam is expected to generate an x-ray focal spot size of ~0.1 to a few micrometers, smaller than conventional ICS x-ray sources [13].

An ICS source can generate a beam with a narrow spectrum, i.e., quasi-monochromatic beam, which helps to avoid streaks and shadow artifacts that arise from the beam hardening of polychromatic spectra [15]. A suitable LPA-ICS source has been developed at the BELLA Hundred Tera Watt (HTW) system under funding from Defense Nuclear Nonproliferation R&D (NA-22). Access to BELLA was facilitated by LaserNetUS. BELLA was configured to produce a stable, quasi-monoenergetic 1 MeV x-ray beam with a small focal spot, a significant step forward from bremsstrahlung sources towards future higher performance CT.

LPAs have previously been used to drive x-ray sources for industrial imaging [16]. There have groups that have used an LPA-ICS source for radiography [17][18] and tomography [19]. In the LPA-ICS source tomography work, the source x-ray energy was about 75 keV.

2. METHODS

2.1 Beamline and Data Acquisition

The beamline schematic is shown in Figure 2. A drive laser creates the plasma wakefield and consequently, the electron beam. The drive laser was a Ti:Sa-based Chirped Laser Amplification (CPA) system. It has a central wavelength of 795 nm, an energy of ~600 mJ, a pulse duration of ~40 fs and a laser focal spot size of 18 µm. A scatter laser interacts with the electron beam to generate x-rays. The scatter laser has similar parameters to the drive laser, except that the energy was 300 mJ.

A sample (also called "object" in this paper) is placed on a rotational stage within the 10^{-4} torr vacuum chamber, about 1 meter from the x-ray focal spot. The x-ray source is optimized to give the highest energy electrons with the narrowest possible spectrum. A magnet placed between the sample and the x-ray source deflects electrons out of the x-ray beam path. An electron spectrometer (not shown) measures the electron spectrum from the deflected electron beam. After the magnet, a thin aluminum foil is used to separate out any unspent laser beam travelling co-linearly with the x-ray beam. Data is measured by a Varian 1611 amorphous silicon flat panel detector. The detector has a gadolinium oxysulphide (GOS) scintillator and 0.1 mm element pitch. It was placed 8 m from the x-ray focal spot. Due to magnification, the effective detector pixel size at the center of rotation is 0.0125 mm.
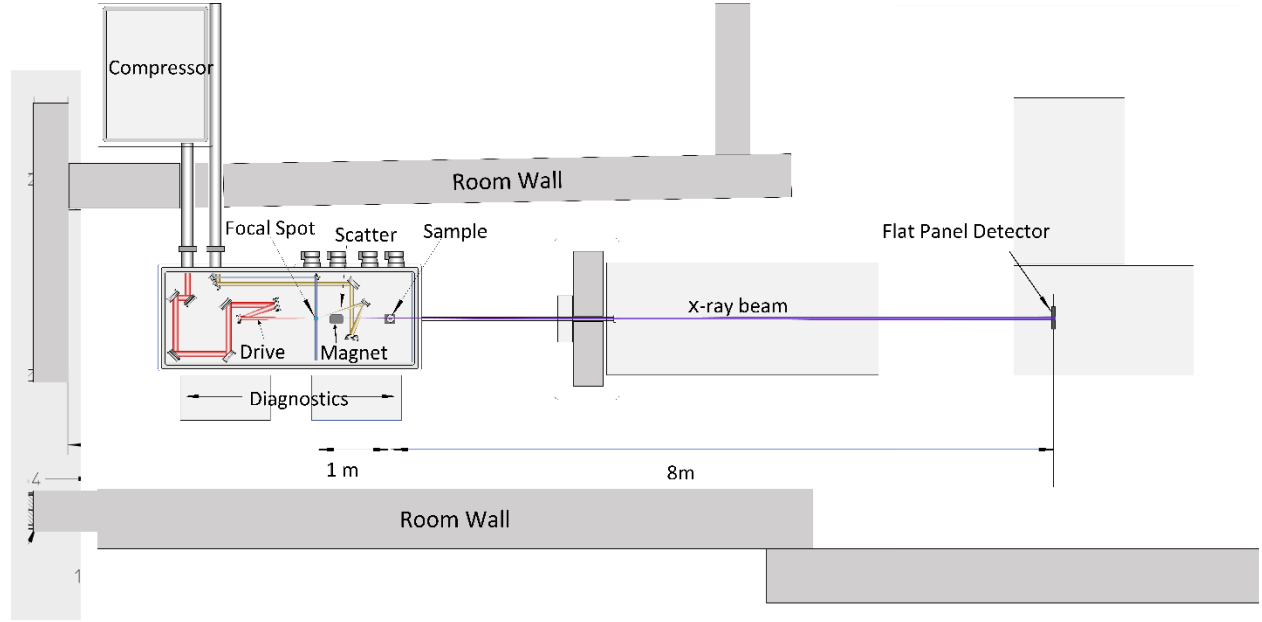
Figure 2. Schematic of the beamline. Pulses from the Drive laser create the wakefield and accelerate electrons. The Scatter laser interacts with the accelerated electrons at the focal spot to produce x-ray photons. A magnet diverts the electron beam out of the x-ray path, and a thin Al foil removes the laser from the path. The deflected electron beam is measured by a spectrometer for diagnostics. X-rays are attenuated by the scanned sample, and incident upon the flat panel detector.

For data acquisition, we installed and integrated sample manipulation stages and a detector with the BELLA LPA-ICS x-ray source. We had four weeks to integrate the stages and detector and to troubleshoot the CT beamline, to optimize the source and to acquire CT data. The CT data were acquired over the last week. We wrote software to rotate the stage, trigger the data acquisition system, and synchronize both with the laser pulses, so that tomographic data could be acquired.

We scanned two objects: a calibration phantom comprising tungsten carbide spheres supported by aluminum stems fabricated at LLNL, a steel bearing manufactured by NSK Motion & Control (Figure 3). The CT data acquisition parameters are given in Table 1. We use the term "frame" to denote one data integration period, and the term "scan" to denote a complete set of frames acquired to image an object. In each scan, multiple frames were acquired at each view position with and without x-rays on. Multiple frames are combined to generate a projection as will be described in detail in the next subsection. We use the notation I_0 to denote the incident beam, i.e., frames and projections with x-rays on when no object is in the x-ray beam. I denotes frames and projections in the scan with x-rays on when an object is in the x-ray beam, and I_d denotes the frames of dark current (x-rays off). The integration time for all frames was 0.5 seconds. I_0 data were collected before and after the object scan. One I_d frame was acquired after each I_0 or I frame. Total scan times per object ranged from 0.5 h for the calibration phantom to 8 h for the steel bearing. The source needed to be stable over these times.
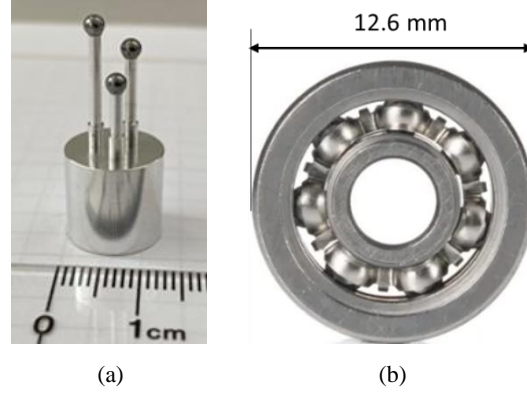
Figure 3. Photographs of test objects scanned. (a) The calibration phantom with 2.5-mm diameter WC spheres mounted on aluminum stems (b) a steel bearing.

Table 1. Nominal data acquisition parameters for an object scan.

Object	Projections	Frames/Projection	Angular Range	Integration Time (s) (I /I_0/I_d)
Calibration phantom	25*	60	288	0.5/0.5/0.5
Bearing	351	60	338	0.5/0.5/0.5

* A small number of projections were obtained since this was our initial scan.

2.2 Data processing and image reconstruction

In each frame, pixels were binned 4 x 4 to increase the signal-to-noise ratio and to reduce read time. Consequently, the effective detector pixel size at the center of rotation was 0.05 x 0.05 mm^2. The I (and I_0) frames were corrected for dark current by subtracting the corresponding I_d frames. The dark-corrected frames at each view position were averaged to generate projections. Log-attenuation projections, denoted P, were generated according to the Beer-Lambert law [20].

$$P = \log\left(\frac{I_0 - I_d}{I - I_d}\right) \tag{1}$$

Median filtering was applied to the log-attenuation projections to reduce outliers. Images were reconstructed with regularized weighted least squares (RWLS) reconstruction, using total variation regularization. The reconstruction was performed using the Livermore Tomography Tools (LTT) software [21]. We customized weights for RWLS for each scan according to the quality of data in each projection, as will be discussed in Section 3. The regularization parameters were manually tuned to reduce noise while maintaining sharp edges. No corrections were applied for beam hardening or scatter reduction.

3. RESULTS AND DISCUSSION

Reconstructed images of one axial slice through each phantom are shown in Figure 4. These are the first high-energy tomographic images acquired using an LPA-ICS. Our initial goal was to acquire, process, and reconstruct CT images. We accomplished this goal, which was a milestone in understanding the application of LPA-ICS sources for CT imaging.
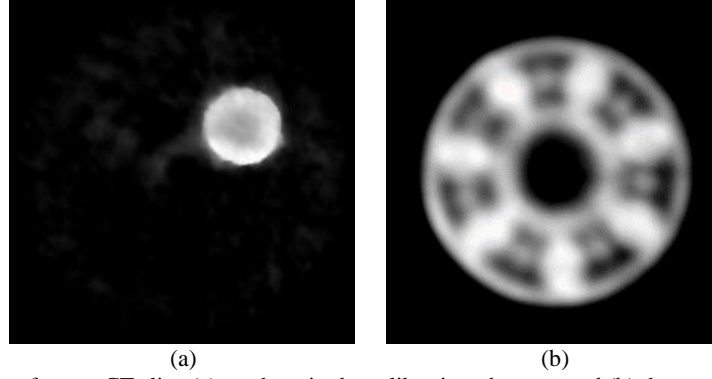
Figure 4. Reconstructed images for one CT slice (a) a sphere in the calibration phantom and (b) the steel bearing.

Figure 5a shows a CT image of a sphere from the calibration phantom, along with a red dashed line and circular region-of-interest (ROI). A profile was plotted along the red dashed line and is shown in Figure 5b. The mean attenuation coefficient within the ROI is 1.02×10^{-2} mm^{-1} and the standard deviation is 1.2×10^{-3} mm^{-1}. We estimated the diameter of this sphere to be 2.4 mm directly from the CT image. This is within 4% of the true value, 2.5 mm.

We estimated the outer diameter of the bearing from the CT slice shown in Figure 4b as 12.16 mm and the inner diameter as 3.04 mm. The outer diameter is within 4% of the true value of 12.6 mm, and the outer diameter is about 1% from its true value. Similar to the calibration phantom sphere, the lengths were estimated directly from the image because a profile plot through the various structures of the bearing is difficult to interpret. For our typical applications, we need dimensional and material accuracies to better than a percent.

Unfortunately, the image quality was poorer than we expected due to problems with the x-ray beam and the detector, and errors in data acquisition. A cupping artifact is visible in the image of the sphere and its profile, as shown in Figure 5. Although the ICS was intended to be a quasi-monochromatic source, estimates of the beam indicated that it was polychromatic. The electron spectrum was measured with a spectrometer and is shown in Figure 6, along with Thomson scatter photon spectra that were estimated by the method of [13]. This calculation yields on-axis photon energies using measured electron energies, while accounting for experimental conditions. The mean energy of this estimated spectrum is 380 keV. For comparison, a bremsstrahlung spectrum from an x-ray tube with 600 kV potential and 2-mm copper filtration yields a mean energy of approximately 250 keV.
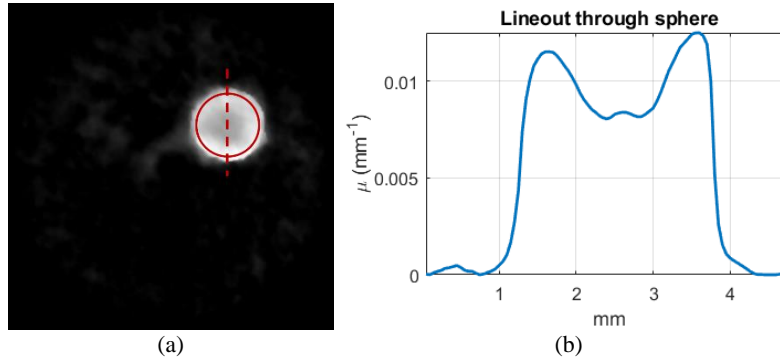

Figure 5. (a) A CT image of a sphere in the calibration phantom, along with a red dashed line and a circular ROI. (b) A profile (lineout) along the red dashed line.
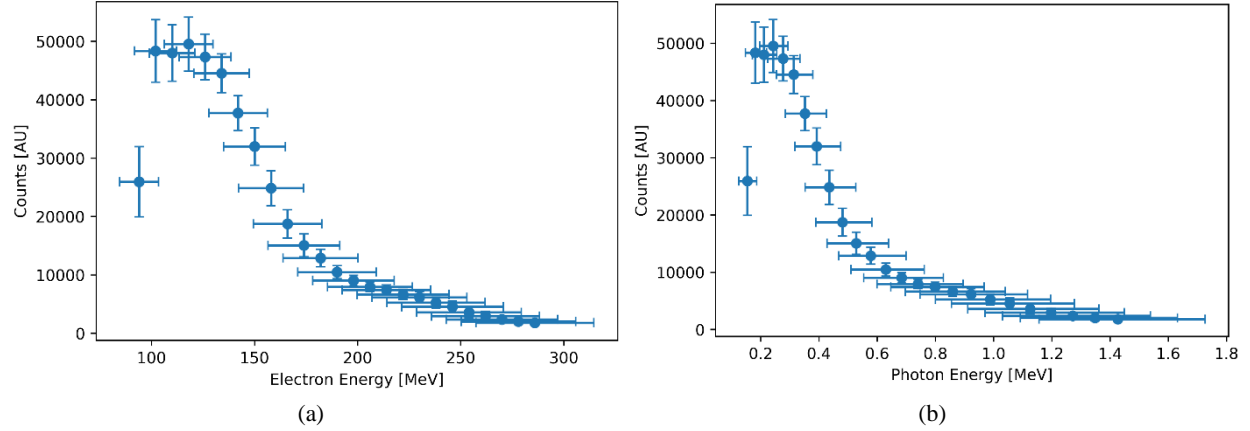
Figure 6. (a) Measured electron spectrum and (b) estimated x-ray spectrum expressed in arbitrary units (AU).

The flux density is low compared to other industrial x-ray sources [15]. The source generates pulses only at 1 Hz (vs kHz envisioned for future applications) and the detector was not optimized for pulsed operation. There were 20-40 counts per frame in the signal $I_0 - I$, and 40-60 frames were averaged per projection. Despite frame averaging, the projection data were noisy. Figure 7a shows a log-attenuation projection, P (Eq. 1), of the calibration phantom. This phantom is suspended from the base and is therefore vertically flipped compared to the photograph in Figure 3. This projection is appropriately corrected and normalized with the I_d and I_0 data respectively. The contrast is large enough to show the three spheres and even the aluminum stems (one is indicated by a yellow arrow) on which they are mounted. Square ROIs within a sphere of the calibration phantom and in air are annotated. Mean values are computed in these ROIs, denoted P_{ball} and P_{air}, respectively. We compute standard deviation for the air ROI, σ_{air}. (It is not meaningful to compute standard deviation in a projection of the sphere, because the x-ray path length through the sphere varies). Larger values of σ_{air} are shown by the spikes in Figure 7b that correspond to projections 7 and 14. The contrast is computed as the difference of means in the ROIs, P_{ball} - P_{air}, and the contrast-to-noise ratio (CNR) is computed as this difference divided by σ_{air}, and is shown in Figure 7c. The CNR is poor compared to industrial scans [15] and decreases with time, which indicates the need for future development of both the LPA-ICS BELLA source and of customized detectors to operate with the pulsed, monochromatic source.
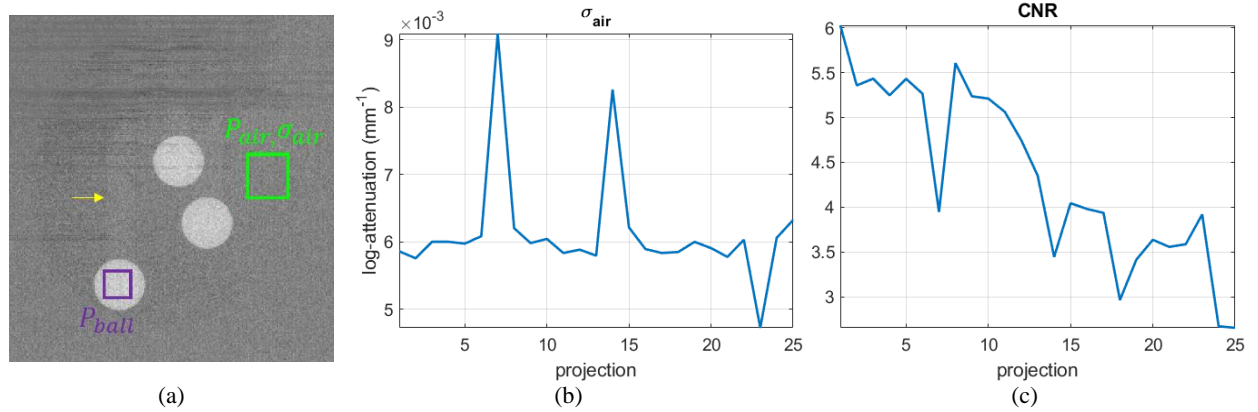

Figure 7. (a) Projection 1 of the calibration phantom is shown along with ROIs in a sphere and in air. (b) Standard deviation in air ROI. (c) The CNR as a function of time.

Projection 23, shown in Figure 8a, shows several data quality issues. Dark horizontal lines degrade this projection. Based on experience, our conjecture is that these lines are due to the low flux-density, which makes the dark current noise in the detector significant. The normalization of Projection 23 with I_0 leaves a residual with magnitude comparable to the object contrast (compared with Projection 1 in Figure 7a). The outer disk defines the field of view of the x-ray beam and should not be distinct from the darker unexposed area of the detector. Although the noise is lower than the other

projections as indicated by the negative spike in Figure 7b, the contrast in this projection is correspondingly low, also suggesting incorrect normalization by I_0.

The contrast between the spheres and air decreases with time (which is proportional to projection number), as demonstrated by lineouts in Figure 8b. There are 25 projections in this scan. Projection 1 shows the greatest contrast between the sphere and air. The contrast is diminished in projection 12, and is the poorest in projection 25. The loss of contrast is also evident in Figure 7c.
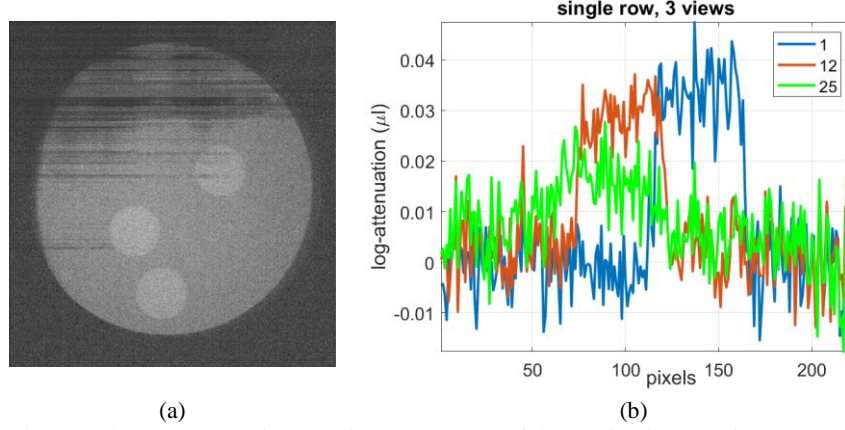

(a)   (b)

Figure 8. (a) Projection 23 shows dark horizontal lines at the top of the projection and incorrect I_0 normalization. (b) One row from Projections 1, 12 and 25 shows the reduction of contrast between the sphere and air.

We designed weighting for the statistical reconstruction according to the quality of the data in each scan. The weights for the reconstruction of the calibration phantom are shown in Figure 9. The weights de-emphasize later projections, as the quality degrades over time.
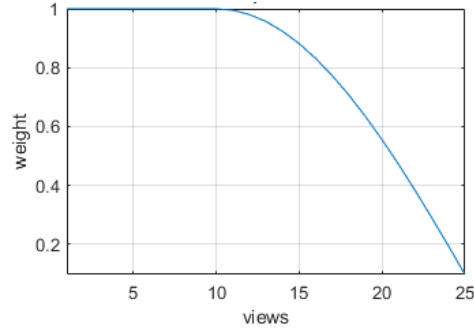

Figure 9. Weights in the RWLS reconstruction algorithm for the reconstruction of the calibration phantom.

We observed that the phantom unexpectedly moved between frames corresponding to a single view position. If uncorrected, this appears as ghosting, as shown in Figure 10. Although the goal in acquisition was 60 frames per view position, we observed in the calibration phantom data that the frames corresponding to different view positions varied from 22 to 301. For the calibration phantom scan, we were able to re-partition the frames into their correct views to remove the ghosting. However, for the bearing we could not re-partition the frames due to the complexity of the object and the larger number of projections. Consequently, ghosting may have persisted and reduced the contrast in reconstructed images.
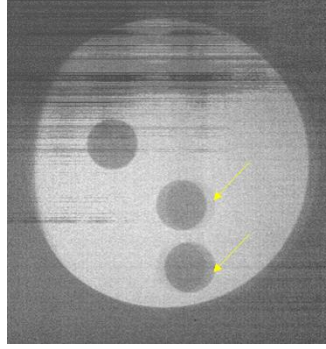
Figure 10 A projection of counts, $I - I_d$ created with the original 60-frame averaging per projection appears to have "ghosted" edges (indicated by arrows) which is caused by the object unexpectedly rotating between frames at a single view position.

The dark current, I_d, drifted during the course of a scan, as shown in Figure 11, although the effect was compensated by using interleaved I_d frames accompanying each frame.
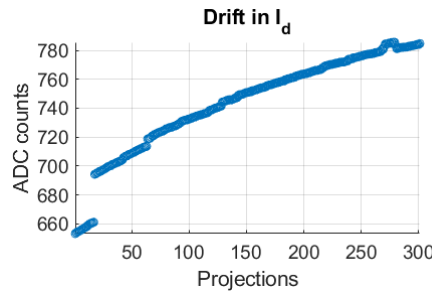

Figure 11. Drift in the dark current, I_d, with projection number, which is proportional to time.

4. FUTURE WORK

We plan to build upon what we learned in these preliminary CT experiments to obtain higher quality CT data at LBNL's BELLA LPA-ICS x-ray source facility. For example, higher flux source, stability over time, and a high-efficiency detector system will improve the projection data quality. The 1611 X-ray panel detector used during the experiment was found to perform poorly for pulsed x-rays and low-flux density. Detector heating may have resulted in greater dark current noise. Better alternatives are available, for example, thermoelectrically cooled scientific CMOS sensors (as used in astronomy applications) would allow longer signal integration times and could be lens-coupled with a high-efficiency scintillator. It would have been helpful to have more diagnostics and monitoring for the rotation stage and the x-ray spectra. It was difficult to access and monitor object motion, and to change samples, since the stages and samples were inside a vacuum.

Efforts are in progress to decrease the BELLA LPA-ICS spectrum bandwidth, increase x-ray energy and provide a more stable beam. These improvements, or work at other LaserNetUS facilities, could allow us to produce an ICS source with higher flux density than those in this experiment, allowing for improved spatial resolution and statistics. Examples of other candidate facilities include:
   •   The DIOCLES (University of Nebraska) laser system: 200 – 700 TW at 0.1 Hz, with the ability to accelerate monochromatic electrons up to 400 MeV. This facility can produce tunable, monochromatic x-rays from 50 keV through 9 MeV.
   •   The Advanced Laser Light Source (Montreal): 150 TW at 2.5 Hz. This facility has a dedicated LPA x-ray beamline which has been used in keV energy range for0 phase contrast imaging and x-ray CT experiments. We can explore applications from keV to MeV energies and produce ICS x-rays using a plasma mirror.
   •   The ALEPH laser (Colorado State University): 1 PW at 3.3 Hz. This facility has also demonstrated the production of x-rays from LPA and could produce ICS x-rays to MeV energies using a plasma mirror.

5. CONCLUSIONS

We have reconstructed the first CT images using an LPA-ICS source with a mean energy of 380 keV. These CT experiments were of a tungsten carbide calibration phantom and a steel bearing. This technology is a promising solution to the problem of imaging industrial objects made from dense metals and containing sub-millimeter structures. The BELLA facility can produce a tunable x-ray beam with MeV energy and micrometer-scale focal spot size. Unfortunately, the x-ray energy and bandwidth were not obtained in the experiments we performed, and the data were noisy and had artifacts. Although we met our initial goal to obtain CT data, we were unable to demonstrate that this source is suitable for tomographic imaging of challenging industrial parts at this time. Our first attempt at using the BELLA LPA-ICS x-ray source helped us understand its potential for NDC, its current performance and required improvements. There are ongoing improvements to the BELLA facility to overcome the current issues. Therefore, we intend to build on our initial results. With the improvements to the BELLA source, changes to the experimental set-up, and rigorous testing, we plan to further explore the benefits of using an LPA-ICS source for NDC.

REFERENCES

[1] Bishop-Moser, J., "Rapid Reliability Assessment of Safety-Critical and Emerging Technologies - Next-Generation Nondestructive Evaluation", Alliance for Manufacturing Foresight, 2019.

[2] Babu, S.S., et al., "Additive Manufacturing of Nickel Superalloys: Opportunities for Innovation and Challenges Related to Qualification", Metall Mater Trans A, 49, p. 3764, 2018.

[3] Talignani, A., et al., A review on additive manufacturing of refractory tungsten and tungsten alloys, Additive Manufacturing 58, 103009, ISSN 2214-8604, https://doi.org/10.1016/j.addma.2022.103009, 2022.

[4] Trapp, J., et al., "In situ absorptivity measurements of metallic powders during laser powder-bed fusion additive manufacturing", Applied Materials Today, Volume 9, Pages 341-349, ISSN 2352-9407, https://doi.org/10.1016/j.apmt.2017.08.006, 2017.

[5] Thompson, A., Maskery, I., and Leach, R., "X-ray computed tomography for additive manufacturing: A review." Measurement Science and Technology, 2016.

[6] Marziani, M., et al., Optimization of radiography applications using x-ray beams emitted by compact accelerators. Part I. Monte Carlo study of the hard x-ray spectrum. Med. Phys., 36: 2009.

[7] Geddes C., et al., "Impact of Monoenergetic Photon Sources on Nonproliferation Applications", Tech. rep., DNN R and D final project report DOI:10.2172/1376659, 2017.

[8] Fazio, M., et al, "Basic Research Needs Workshop on Compact Accelerators for Security and Medicine: Tools for the 21st Century", Technical Report for USDOE Office of Science, (2019).

[9] H. R. Weller, M. W. Ahmed, H. Gao, W. Tornow, Y. K. Wu, M. Gai and R. Miskimen, "Research opportunities at the upgraded HIγS facility.", Proc. Part. Nucl. Phys., 62, p. 257 2009.

[10] Albert, F., et al., "Laser Wakefield Accelerators: Next-Generation Light Sources", Optics & Photonics News - Laser Wakefield Accelerators: Next-Generation Light Sources (optica-opn.org).

[11] Bingham, R., and Trines, E., "Introduction to Plasma Accelerators: the Basics", In Proceedings of the CAS-CERN Accelerator School: Plasma Wake Acceleration, Geneva, Switzerland, 23–29, November 2014.

[12] G.R.Plateau, et al., "Low-Emittance Electron Bunches from a Laser-Plasma Accelerator Measured using Single-Shot X-Ray Spectroscopy," Phys. Rev. Lett. 109, 064802, 2012.

[13] Rykovanov, S.G., et al., "Quasi-monoenergetic femtosecond photon sources from Thomson Scattering using laser plasma accelerators and plasma channels", Journal of Physics B: Atomic, Molecular and Optical Physics, 47., 2014.

[14] Corde, S., et al., "Femtosecond x rays from laser-plasma accelerators", Reviews of Modern Physics, 85, JANUARY–MARCH 2013.

[15] Martz, H., et al., "X-Ray Imaging: Fundamentals, Industrial Techniques and Applications", CRC Press, ISBN 9781315375199, 2016.

[16] J.-N. Gruse, "Application of compact laser-driven accelerator X-ray sources for industrial imaging", Nuclear Instruments and Methods in Physics Research Section A: Accelerators, Spectrometers, Detectors and Associated Equipment, Volume 983,164369, 2020.

[17] A Döpp, et al., "An all-optical Compton source for single-exposure x-ray imaging," Plasma Phys. Control. Fusion 58 034005, 2016.

[18] Haden, D. "High-resolution radiography of thick steel objects using an all-laser-driven MeV-energy x-ray source", Advances in Laboratory-Based X-Ray Sources, Optics, and Applications V [99640G] (Proceedings of SPIE - The International Society for Optical Engineering), 2016.

[19] Yue Ma, "Region-of-interest micro-focus computed tomography based on an all-optical inverse Compton scattering source", Matter and Radiation at Extremes 5, 064401, 2020.

[20] Swinehart, D.F., The beer-lambert law. Journal of chemical education, 39(7), p.333, 1962.

[21] Champley, K., et al., "Livermore Tomography Tools: Accurate, Fast, and Flexible Software for Tomographic Science", NDT & E International, 2021.